Jurnal Reka Lingkungan
ISSN(p): 2337-6228 | ISSN(e): 2722-6077 | Vol. 14 | No. 2 | Hal. 187 - 204
DOI: http://dx.doi.org/10.26760/rekalingkungan.v14i2.187-204 Agustus 2026

NUMERICAL STUDY OF O_2/RFG EFFECTS ON COMBUSTION BEHAVIOR AND EMISSIONS IN A 60 MWe OXY-FUEL CIRCULATING FLUIDIZED BED BOILER

FANDY ARIDHA PERBAWAJAYA[1], IS BUNYAMIN SURYO[1]

1. Mechanical Engineering Department, Institut Teknologi Sepuluh Nopember, Sukolilo, Surabaya, 60111
Email : fandy.aridha@gmail.com

ABSTRAK

Indonesia menargetkan Net Zero Emission (NZE) pada 2060 melalui dekarbonisasi sektor energi. Sebagai solusi transisi, teknologi Penangkapan, Pemanfaatan, dan Penyimpanan Karbon (CCUS), khususnya pembakaran oxy-fuel, menawarkan jalan untuk menyeimbangkan pengurangan emisi dengan keamanan energi. Penelitian ini mengevaluasi penerapan oxy-fuel pada boiler Circulating Fluidized Bed (CFB) 60 MWe PLTU Pulang Pisau menggunakan Ansys Fluent 2025 R1 dengan mengganti nitrogen (N_2) menjadi karbon dioksida (CO_2) kering. Dengan menjaga laju batu bara dan oksigen tetap konstan, hasilnya menunjukkan peningkatan suhu bed (7.45%) dan outlet siklon (8.37%). Karakteristik termal ini mendorong lonjakan konsentrasi CO_2 sebesar 325.12%, sekaligus mereduksi emisi SO_2 (43.17%) dan NO_x (13.88%). Penelitian ini menegaskan kelayakan teknis untuk memodifikasi unit CFB yang ada dengan teknologi oxy-fuel, memberikan wawasan penting tentang bagaimana perubahan moda pembakaran memengaruhi kinerja termal dan profil emisi selama transisi menuju produksi energi yang lebih bersih.

***Kata kunci**: penangkapan karbon, Boiler CFB, pengurangan emisi, simulasi numerik, pembakaran oxy-fuel*

ABSTRACT

Indonesia aims to achieve Net Zero Emissions (NZE) by 2060 through the decarbonization of its energy sector. As a transitional solution, Carbon Capture, Utilization, and Storage (CCUS) technology, specifically oxy-fuel combustion, offers a viable pathway to balance emission reductions with energy security. This study evaluates the implementation of oxy-fuel combustion in a 60 MWe Circulating Fluidized Bed (CFB) boiler at the Pulang Pisau Thermal Power Plant using Ansys Fluent 2025 R1 by replacing nitrogen (N2) with dry carbon dioxcide (CO2). By maintaining constant coal feeding and oxygen supply rates, the results demonstrate increases in bed temperature (7.45%) and cyclone outlet temperature (8.37%). These enhanced thermal characteristics drive a sharp surge in CO2 concentration by 325.12%, while simultaneously reducing SO2 and NOx emissions by 43.17% and 13.88%, respectively. This research confirms the technical feasibility of retrofitting existing CFB units with oxy-fuel technology, providing valuable insights into how mode-switching affects thermal performance and emission profiles during the transition toward cleaner energy production.

***Keywords**: carbon capture, CFB boiler, emission reduction, numerical simulation, oxy-fuel combustion*

1. INTRODUCTION

Indonesia has positioned itself as a key global actor in climate change mitigation by pledging to attain Net Zero Emissions (NZE) by 2060 or earlier (Ministry of Environment and Forestry of the Republic of Indonesia, 2021). This foundational pledge originated from the ratification of the Paris Agreement in 2016 and was further fortified through the Enhanced Nationally Determined Contribution (E-NDC) in 2022. Under this updated framework, Indonesia committed to an unconditional greenhouse gas (GHG) reduction target of 31.89%, which could rise to 43.20% subject to international assistance by 2030 (Ministry of Environment and Forestry of the Republic of Indonesia, 2022). To realize this goal, PT Perusahaan Listrik Negara (Persero)—or PLN—launched a cornerstone transformation program in 2022 termed the "NZE Moonshot." This forward-looking initiative marks a paradigm shift from fossil-fuel reliance toward sustainable clean energy, highlighting PLN's role in advancing the national energy transition and green growth (PLN, 2021). Beyond decarbonization, this strategic overhaul aims to restructure the national grid to ensure energy equity, fairness, and public welfare.

Reaching the NZE 2060 milestone necessitates deep decarbonization across the power sector, which remains predominantly driven by coal-fired power plants. Nevertheless, accelerating the retirement of coal assets—including newly built units—encounters significant barriers. Financial hurdles center on compensation liabilities under Independent Power Producer (IPP) agreements and the threat of stranded assets burdening public finances. From a technical standpoint, coal-fired units deliver essential baseload power; thus, premature decommissioning without mature renewable alternatives risks destabilizing the grid and triggering power shortages. To reconcile ambitious decarbonization goals with grid reliability and economic stability, Carbon Capture, Utilization, and Storage (CCUS) emerges as a vital bridging technology (International Energy Agency, 2022).

CCUS is widely recognized as a pivotal tool in global decarbonization, capable of intercepting carbon dioxide (CO_2) emissions from heavy industry and energy-intensive systems (IPCC, 2005). According to the IPCC Special Report (2005), flue gas from coal-fired power plants exhibits a dry CO_2 concentration of around 12–14% by volume, which holds significant potential for carbon capture implementation. The captured carbon can either be repurposed for commercial applications or permanently trapped within deep geological formations. As a result, CCUS serves as an indispensable solution for hard-to-abate sectors to sustain industrial output while drastically reducing emissions (IPCC, 2022). In fossil-fuel-based power generation, CCUS adoption generally follows three main routes: pre-combustion, post-combustion, and oxy-fuel combustion (Chen et al., 2023).

The core mechanism of oxy-fuel combustion relies on burning fuel in an oxygen-rich environment, producing a flue gas stream enriched with high-purity CO_2 that simplifies downstream capture (IPCC, 2005). Consequently, this technology has gained substantial traction for commercial-scale CCUS integration. As depicted in Figure 1, a CCUS-integrated circulating fluidized bed oxy-fuel combustion (Oxy-CFBC) plant typically integrates four key units: an Air Separation Unit (ASU) for oxygen supply, a CFB boiler serving as the main furnace, a flue gas cleaning unit for pollutant removal, and a Compression Purification Unit (CPU) to condense the CO_2 into a storage-ready state (Zheng & Liu, 2018). To regulate furnace temperatures and control heat transfer, conventional combustion air is replaced by recirculating a significant portion of Recycled Flue Gas (RFG) mixed with pure oxygen supplied by the ASU. Although RFG generally contains combustion by-products including CO_2, water vapor (H_2O), nitrogen oxides (NO_x), sulfur dioxide (SO_2), and ash, it consists

primarily of CO_2 in an Oxy-CFBC system owing to the systematic removal of nitrogen, sulfur, and moisture via the ASU, limestone injection, and flue gas coolers.

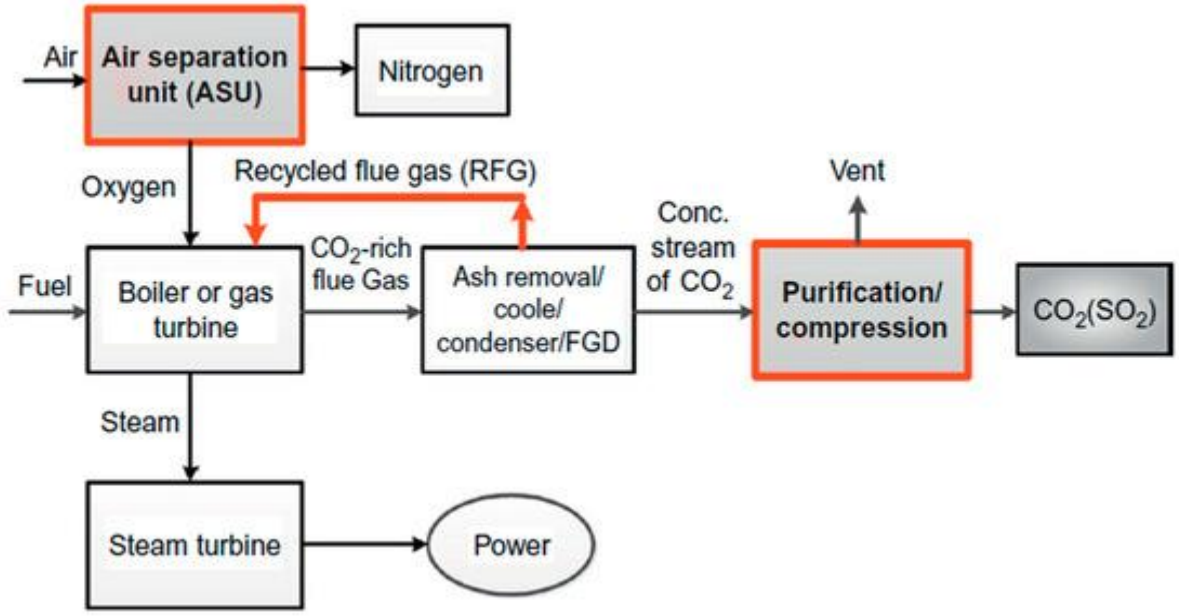

Figure 1. General schematic of CCUS integrated Oxy-CFBC (Zheng and Liu, 2018)

Implementing oxy-fuel combustion technology by replacing N_2 with CO_2 substantially alters the thermophysical characteristics and fluid heat transfer behavior. This shift stems from fundamental differences in molecular structure, molecular weight, and thermodynamic properties between diatomic N_2 and triatomic CO_2 molecules. Unlike N_2, whose vibrational modes remain relatively passive at low to moderate temperatures, CO_2 possesses more quantized vibrational modes (bending and stretching) that are readily excited at lower energy levels (Buhre et al, 2005). The presence of these internal vibrational modes enables CO_2 to store a greater amount of thermal energy, resulting in both molar and mass specific heat capacities (C_p) that surpass those of N_2 at elevated combustion temperatures. Coupled with the higher molar mass of CO_2 (44 g/mol vs. 28 g/mol for N_2), the O_2/CO_2 mixture exhibits a higher thermal inertia, ultimately suppressing the adiabatic flame temperature compared to conventional O_2/N_2 combustion systems. (Toftegaard et al, 2010)

Advancing clean combustion technologies in power generation depends heavily on a detailed understanding of the furnace's thermal behavior, hydrodynamics, and emission characteristics. Previous studies have actively sought to model these phenomena; for example, the Multiphase Particle-in-Cell (MP-PIC) method in Barracuda was applied by Gu et al. (2019) to evaluate the changes in combustion characteristics of air and oxy-fuel in a 15 kW_{th} lab-scale facility, while Raheem et al. (2021) observed a fourfold increase in bed temperature during O2/RFG combustion in a 30 kW_{th} bench-scale system. Furthermore, Dong et al. (2024) evaluated the effects of O_2/RFG concentration in a lab-scale bubbling fluidized bed (BFB) facility using anthracite coal. Meanwhile, experimental investigations were conducted by Yang et al. (2020) on a 0.1 MW_{th} bench-scale unit to examine the combustion and emission characteristics during the transition from air-firing to oxy-fuel mode.

While prior research offers a solid theoretical foundation on oxy-fuel kinetic mechanisms, a notable gap remains in translating these findings to real-world industrial scale-up. Existing studies predominantly focus on simplified geometries or bench-scale laboratory setups,

leaving large-scale thermal radiation dynamics and core-annulus solids transport under-represented. Crucially, available computational models have not yet incorporated the unique properties of Indonesian low-rank coals—such as high moisture and elevated reactivity—which are extensively fired in regional power plants. This gap creates operational uncertainties, particularly regarding bed clinkering induced by localized thermal spikes observed in small-scale tests. To address these limitations, this study conducts a comprehensive 3D numerical assessment to evaluate the combustion behavior of an industrial CFB boiler. By focusing on the 60 MWe Pulang Pisau Power Plant, this work provides critical insights into the operational characteristics of retrofitted domestic fossil-fuel facilities.

2. MATERIALS AND METHODS

2.1. Numerical model setup

The numerical model was constructed within the ANSYS™ Workbench environment utilizing the Fluent solver, incorporating the exact spatial dimensions of the physical test facility. To simulate the 200-ton/hour CFB boiler, a comprehensive 3-Dimensional mathematical framework was implemented using Computational Fluid Dynamics (CFD) methods. This model captures both homogeneous and heterogeneous combustion within the reactive mixture flow. The finite volume method was employed to solve the governing equations for mass, momentum, enthalpy, and the specific gaseous species involved in the combustion process. Turbulence effects were modeled using the Reynolds-averaged Navier–Stokes (RANS) equations paired with the k-ϵ Realizable turbulence model, while heat transfer along the combustion chamber walls was resolved through coupled convection and radiation models. The solid-phase granular behavior was simulated using an Euler-Euler multiphase model, with silica sand serving as the bed material. Here are the fundamental governing equations formulated for a combustion gas-phase flow solved using the Finite Volume Method under the RANS framework.

2.1.1. Conservation of mass (Continuity equation)

This equation ensures the conservation of total mass within the system. A mass source term S_m is added to account for the mass transferred from the solid phase (coal) to the gas phase during devolatilization or char gasification (Ansys, 2025).

$$\frac{\partial \rho}{\partial t} + \frac{\partial}{\partial x_i}(\rho \bar{u}_i) = S_m \quad \text{.....(1)}$$

where $\rho, \bar{u}_i, S_m$ are mixture gas density, mean velocity component in the i-direction, and mass source term from the discrete particle phase, respectively.

2.1.2. Conservation of momentum (RANS equations)

This equation governs the forces acting on the fluid flow, where the effect of turbulent fluctuations is accounted for by the Reynolds stress tensor ($-\rho\overline{u'_i u'_j}$) (Ansys, 2025).

$$\frac{\partial}{\partial t}(\rho \bar{u}_i) + \frac{\partial}{\partial x_j}(\rho \bar{u}_i \bar{u}_j) = -\frac{\partial p}{\partial x_i} + \frac{\partial}{\partial x_j}\left[\mu\left(\frac{\partial \bar{u}_i}{\partial x_j} + \frac{\partial \bar{u}_j}{\partial x_i} - \frac{2}{3}\delta_{ij}\frac{\partial \bar{u}_k}{\partial x_k}\right)\right] + \frac{\partial}{\partial x_j}\left(-\rho\overline{u'_i u'_j}\right) + S_F \text{ ...(2)}$$

Using the Boussinesq hypothesis, the Reynolds stresses are modeled as:

$$-\rho\overline{u'_i u'_j} = \mu_t\left(\frac{\partial \bar{u}_i}{\partial x_j} + \frac{\partial \bar{u}_j}{\partial x_i}\right) - \frac{2}{3}\left(\rho k + \mu_t \frac{\partial \bar{u}_k}{\partial x_k}\right)\delta_{ij} \quad \text{.....(3)}$$

where p, μ, μ_t, S_F are static pressure, molecular dynamic viscosity, turbulent viscosity (*eddy viscosity*) and external force source term.

2.1.3. Conservation of energy (Static enthalpy equation)

This equation describes the thermal energy distribution throughout the furnace, resolving heat transport via convection, diffusion, and heat release (Ansys, 2025).

$$\frac{\partial}{\partial t}(\rho h) + \frac{\partial}{\partial x_i}(\rho \bar{u}_i h) = \frac{\partial}{\partial x_i}\left(k_{eff}\frac{\partial T}{\partial x_i}\right) - \frac{\partial}{\partial x_i}\left(\sum_j h_j J_j\right) + S_{hr} + S_{rad} + S_{hp} \quad \text{.....(4)}$$

which $h, k_{eff}, J_j,$ were static enthalpy of the mixture, effective thermal conductivity ($k + k_t$, where $k_t = \frac{C_p \mu_t}{Pr_t}$) and diffusion flux of species j. Then S_{hr}, S_{rad}, S_{hp} were source term due to chemical heat release from combustion, radiation heat source/sink term ($\nabla \cdot q_{rad}$) and interphase heat exchange with the solid/particle phase, respectively.

2.1.4. Species transport equation

To track the local mass fraction of each chemical species (O_2, N_2, CO_2, H_2O, etc.) involved in the combustion process (Ansys, 2025).

$$\frac{\partial}{\partial t}(\rho Y_i) + \frac{\partial}{\partial x_j}(\rho \bar{u}_j Y_i) = -\frac{\partial}{\partial x_j} J_{i,j} + R_i + S_{p,i} \quad \text{.....(5)}$$

Where the turbulent diffusion flux is modeled using Fick's Law approximation:

$$J_{i,j} = -\left(\rho D_{m,i} + \frac{\mu_t}{Sc_t}\right)\frac{\partial Y_i}{\partial x_j} \quad \text{.....(6)}$$

where Y_i, $D_{m,i}$, Sc_t, R_i, $S_{p,i}$ are mass fraction of species i, molecular mass diffusion coefficient, turbulent Schmidt number (typically set to 0.7 in Ansys Fluent), net rate of production/consumption of species i due to chemical reactions, and mass source term from the discrete phase (e.g., volatile gas release), respectively.

2.1.5. Realizable $k - \epsilon$ turbulence model

The turbulent viscosity is closed using the relationship $\mu_t = \rho C_\mu \frac{k^2}{\epsilon}$. The transport equations for the turbulent kinetic energy (k) and its dissipation rate (ϵ) are defined as:

- Turbulent kinetic energy (k) equation:

$$\frac{\partial}{\partial t}(\rho k) + \frac{\partial}{\partial x_j}(\rho k \bar{u}_j) = \frac{\partial}{\partial x_j}\left[\left(\mu + \frac{\mu_t}{\sigma_k}\right)\frac{\partial k}{\partial x_j}\right] + G_k + G_b - \rho\epsilon \quad \text{.....(7)}$$

Turbulent dissipation rate (ϵ) equation:

$$\frac{\partial}{\partial t}(\rho \epsilon) + \frac{\partial}{\partial x_j}(\rho \epsilon \bar{u}_j) = \frac{\partial}{\partial x_j}\left[\left(\mu + \frac{\mu_t}{\sigma_\epsilon}\right)\frac{\partial \epsilon}{\partial x_j}\right] + \rho C_1 S\epsilon - \rho C_2 \frac{\epsilon^2}{k + \sqrt{\nu\epsilon}} \quad \text{.....(8)}$$

Unlike the *Standard* $k - \epsilon$ model, C_μ is not a constant (0.09) but a variable mathematical function of the strain rate and mean rotation. This mathematical constraint satisfies certain realizability conditions, preventing non-physical negative normal stresses (Ansys, 2025).

2.1.6. Radiation heat transfer model (Source term S_{rad})

To resolve radiative heat transfer and couple it with the combustion chamber walls, standard differential models like the Discrete Ordinates (DO) model are utilized. For example, the The formal DO radiation transport equation for a non-scattering or scattering medium is expressed as (Ansys, 2025):

$$\nabla \cdot (I(\vec{r}, \vec{s})\vec{s}) + (a + \sigma_s) I(\vec{r}, \vec{s}) = an^2 \frac{\sigma T^4}{\pi} + \frac{\sigma_s}{4\pi}\int_0^{4\pi} I(\vec{r}, \vec{s}')\Phi(\vec{s} \cdot \vec{s}')d\Omega' \quad \text{.....(9)}$$

where $\vec{r}, \vec{s}, \vec{s}', I(\vec{r}, \vec{s}), a, \sigma_s$ are position vector, direction vector, scattering direction vector, radiation intensity, gas absorption coefficient, and scattering coefficient. Then n, σ, T, Φ, Ω' are refractive index, Stefan-Boltzmann constant (5,67 x 10^{-8} W/m^{2}K^4), local temperature, phase function, and solid angle, respectively.

2.2. Coal combustion process and chemical reaction model

Fuel fed into a CFB system undergoes a sequential series of combustion stages. As detailed by Basu (2015), these stages include preheating and drying, devolatilization followed by the

combustion of volatile matters, swelling and primary fragmentation (for certain coal types), and char combustion accompanied by secondary fragmentation and particle attrition. Upon entering the CFB furnace, the fresh fuel immediately mixes with a massive volume of hot, inert solid particles (bed sand). This direct contact allows the hot sand to act as an effective preheating medium, rapidly raising the fuel particle temperature close to the operating bed temperature. In general, the coal drying process can be represented by the following chemical equation: (Lian et al., 2025)

$$H_2O_{(l)} \rightarrow H_2O_{(g)} \quad (10)$$

While fuel drying is a highly complex phenomenon heavily governed by the local heat and mass transfer characteristics within the reactor, it takes place almost instantaneously. Consequently, in numerical modeling, it is reasonable to neglect this rapid drying phase to simplify the simulation. The second stage is devolatilization, also known as pyrolysis, refers to the thermal decomposition of fuel that liberates a variety of gaseous products, encompassing both condensable and non-condensable fractions (Basu, 2015). Volatile matter is primarily composed of various hydrocarbons that are liberated progressively. Within a coal particle, this sequential devolatilization exhibits an initial, steady release between 500–600°C, followed by a second devolatilization phase occurring within the 800–1000°C range. The devolatilization process itself can be expressed by the following reaction sequence (Lian et al., 2025).

$$\text{Fuel}(s) \rightarrow \alpha_1\text{Char}(s) + \alpha_2\text{Volatiles}(g) + \alpha_3\text{Ash}(s) \quad (11)$$

$$\text{Volatiles}(g) \rightarrow \alpha_1\text{CO} + \alpha_2\text{CO}_2 + \alpha_3\text{CH}_4 + \alpha_4\text{H}_2 + \alpha_5\text{H}_2\text{O} + \alpha_6\text{HCN} + \alpha_7\text{NH}_3 + \alpha_8\text{H}_2\text{S} + \alpha_9\text{N}_2 + \alpha_{10}\text{Tar} \quad (12)$$

Volatile combustion is a critical constituent of the overall combustion process, occurring either prior to or concurrently with char oxidation. This phenomenon significantly influences the efficiency and kinetic dynamics of the subsequent char combustion system. Research consistently indicates that volatile oxidation enhances char combustion by providing auxiliary heat and generating reactive radicals, which accelerate the decomposition of the char matrix. The primary volatile species evolved during coal combustion include CO, H_2, CH_4, and tar. The chemical pathways governing volatile combustion are represented by the following reaction equations: (Lian et al., 2025)

$$\text{CO} + 0.5\text{O}_2 \rightarrow \text{CO}_2 \quad (13)$$

$$\text{H}_2 + 0.5\text{O}_2 \rightarrow \text{H}_2\text{O} \quad (14)$$

$$\text{CH}_4 + 2\text{O}_2 \rightarrow \text{CO}_2 + 2\text{H}_2\text{O} \quad (15)$$

$$\text{CH}_4 + 1.5\text{O}_2 \rightarrow \text{CO} + 2\text{H}_2\text{O} \quad (16)$$

$$\text{C}_x\text{H}_y\text{O}_z\text{N}_l\text{S}_n\ (\text{Tar}) + \left(\frac{x}{2} + \frac{y}{4} - \frac{z}{2} + n\right)\text{O}_2 \rightarrow x\text{CO} + \frac{y}{2}\text{H}_2\text{O} + \frac{l}{2}\text{N}_2 + n\text{SO}_2 \quad (17)$$

The next stage involves char combustion, which generally begins once the volatiles have been released and takes the most time to complete. During the combustion of char particles, oxygen from the furnace air stream is carried to the particle surface. The oxygen then reacts through oxidation with the carbon on the surface. Additionally, if conditions are favorable, it can diffuse into the pores to produce combustion products such as CO and CO_2, as described by the following equations: (Lian et al., 2025)

$$\text{C}_{(s)} + \frac{1}{2}\text{O}_2 \rightarrow \text{CO} \quad (18)$$

$$\text{C}_{(s)} + \text{O}_2 \rightarrow \text{CO}_2 \quad (19)$$

The five-step reactions (4-8) are used for the homogeneous combustion the volatiles, and the multiple surface reaction model with two-step heterogeneous reactions (9–10) are considered for the char burnout. The Arrhenius kinetic parameters, activation energy and mass diffusion-limited constant (Ci) of different reactions are shown in Table 1. Ci is different

for air-combustion and oxy-combustion because of the different diffusivities in the N_2-rich or CO_2-rich environment. (Li et al, 2024). All the homogenous gas-phase reactions have been considered as the fast chemistry processes. Reaction rates were calculated based on the Eddy Dissipation approach.

Table 1. The Arrhenius number, activation energy and mass diffusion-limited constant of different reactions (Li et al, 2024)

Reaction	Arrhenius Number (kmol/m^{3}s)	Activation Energy (J/kmol)	mass diffusion-limited constant, Ci (-)
(4)	2.239×10^{12}	1.7×10^{8}	-
(5)	9.87×10^{8}	3.1×10^{7}	-
(6)	1.6×10^{10}	1.67×10^{8}	-
(7)	4.4×10^{11}	1.25×10^{8}	-
(8)	2.119×10^{11}	2.027×10^{8}	-
(9)	0.005	7.4×10^{7}	[a] 5.32×10^{-12} / [b] 4.13×10^{-12}
(10)	0.002	7.9×10^{7}	[a] 5.06×10^{-12}/ [b] 4.0×10^{-12}
[a] for air firing combustion ; [b] for oxy-fuel combustion			

2.3. NO_x model

The mathematical model for NO_x is employed to project the cumulative formation of NO_x inside the CFB boiler. This integrated model configures emission parameters by accounting for thermal NO_x and fuel NO_x, structured as follows: Thermal NO_x generation is governed by a series of chemical reactions that are highly sensitive to temperature fluctuations, commonly known as the extended Zeldovich mechanism which is written in the following equation (Bryden et al, 2022):

$$O + N_2 \rightleftharpoons N + NO \quad \text{.....(20)}$$
$$N + O_2 \rightleftharpoons O + NO \quad \text{.....(21)}$$
$$N + OH \rightleftharpoons H + NO \quad \text{.....(22)}$$

The fundamental reactions controlling thermal NO_x formation from molecular nitrogen require estimated concentration data for O atoms and OH free radicals, alongside the availability of stable chemical species. In this modeling approach, the concentrations of both radical species are assumed to satisfy partial-equilibrium conditions. Fuel NO_x accounts for the emissions liberated during the coal combustion process, originating from the fuel-bound nitrogen residing within both the volatile matter and the char matrix. At specific temperature thresholds, volatile-bound nitrogen reacts to form intermediate compounds, typically HCN and NH_3. A portion of these intermediates undergoes oxidation by oxygen to generate NO_x, whereas the remaining fraction reacts with the already formed NO_x through a reduction pathway to yield stable N_2. Concurrently, char-bound nitrogen (Char-N) reacts directly with oxygen to produce NO_x without transitioning through intermediate products; however, a minor fraction of this generated NO_x is subsequently reduced back to N_2 via heterogeneous reactions on the char surface.

2.4. Material properties and boundary conditions

The fluid domain was specified as a multi-component reacting mixture incorporating local mass fractions of N_2, H_2O, CO_2, O_2, and devolatilized species. Sub-bituminous coal (properties listed in Table 2) was utilized as the solid fuel. Primary fuel particles were assigned a density, specific heat, moisture evaporation threshold, and mean diameter of 1310 kg/m^3, 1600 J/(kg · K), 400℃, and 5 mm, respectively. Meanwhile, the inert bed

material was set with a density of 2320 kg/m^3, a specific heat capacity of 691 J/(kg · K), and a mean diameter of 2 mm. Thermal boundary conditions at the combustor walls fully incorporated both convective and radiative heat transfer modes. The corresponding parameter distributions are summarized in Table 3 and illustrated in Figure 2.
The boundary and initial conditions for the simulation were defined as follows:

- **Primary air**
  Configured as a pressure inlet for the oxidizer at a temperature of 230°C and a turbulence intensity of 5%. Within this primary air stream, the effect of the air-firing combustion mode—configured with an inlet concentration of 21% O_2 + 79% N_2—will be investigated and compared against the oxy-firing mode featuring a composition of 21% O_2 + 79% RFG (primarily CO_2). To optimize computational efficiency, the geometric complexity of the air nozzle caps was substituted with a porous media zone featuring a porosity of 0.57.
- **Secondary air**
  Introduced through sixteen distinct inlets, each with a hydraulic diameter of 0.2267 m. The air supply across these inlets ranges from approximately 3.0 to 4.6 kg/s, with operating temperatures spanning 206°C to 233°C and a baseline turbulence intensity of 5%. The composition of the secondary air is maintained constant using air as the oxidizer
- **Domain outlets**
  Designated as two exit boundaries routing flow from the cyclones to the backpass. These outlets are characterized by a hydraulic diameter of 3.451 m, a negative gauge pressure of -780 Pa, and a turbulence intensity of 5%.
- **Fuel and bed inventory**
  Administered via four feeders delivering a cumulative fuel flow rate of 40 t/h. The total active inventory mass of the fluidized bed was set to 52 tons, with no limestone or alternative sorbent additives included in this study.
- **Boundary wall**
  Five boundary walls, which the material is carbon steel SA210, consisting of the front, rear, right, and left wall tubes, as well as the wingwall, are utilized to absorb combustion heat. This thermal energy is transferred to evaporate feedwater, maintaining a flow rate of 200 tons/hour under a drum pressure of 9.15 MPa. The rest of the boundary wall consists mostly of refractory material, which serves to safeguard the boiler from thermal and erosive damage.

Table 2. Analysis of sub-bituminous coal consumed in the Pulang Pisau CFB boiler

Proximate (AR)	%	Ultimate (ADB)	%
Volatile	32,69	C	54,29
Fixed Carbon	29,48	H	6,47
Ash	3,67	O	33,79
Moisture	34,16	N	0,79
Gross Calorific Value (AR)	4176 kCal/kg	S	0,22

2.5. Numerical Approach for Fluidized Bed Dynamics

Fluidized bed hydrodynamics were modeled using a pressure-based solver formulation, where velocity fields are resolved through a pressure-correction equation derived from the conservation of mass and momentum. Although the Pulang Pisau Power Plant features a rated nameplate capacity of 60 MWe, its official operating baseline under the Power

Purchase Agreement (PPA) with PT PLN (Persero) is set at a Net Dependable Capacity of 45 MWe net, which corresponds to a 54 MWe gross output. To accurately reflect these real-world thermophysical boundary conditions, the validation of boiler temperature and pressure profiles was conducted using historical operational data at a 54 MWe gross load, with numerical simulations executed under the same operating state. To resolve the governing transport equations, a robust solver architecture was configured in ANSYS™ Fluent to balance numerical stability, execution speed, and physical accuracy. Pressure-velocity coupling was achieved via the Coupled algorithm, which simultaneously solves the continuity and momentum equations to expedite convergence in tightly coupled flow regimes. For spatial discretization, cell gradients were computed using the Green-Gauss Cell-Based scheme, whereas the PRESTO! (PREssure STaggering Option) scheme was employed for pressure discretization to capture the steep pressure gradients typical of fluidized bed systems. High-order spatial accuracy for momentum, turbulent kinetic energy, dissipation rate, energy, and chemical species fractions was maintained using the Second-Order Upwind scheme to reduce numerical diffusion. To maintain numerical stability and avoid divergence in highly non-linear reaction calculations, explicit under-relaxation factors were set to 0.25. Convergence was assessed by enforcing a residual threshold of 10^{-3} for hydrodynamic and species transport equations, alongside a stricter criterion of 10^{-6} for the energy equation to ensure exact thermal equilibrium. Finally, the flow domain was initialized using the hybrid initialization technique to establish a physically consistent starting field prior to the main iterative process.

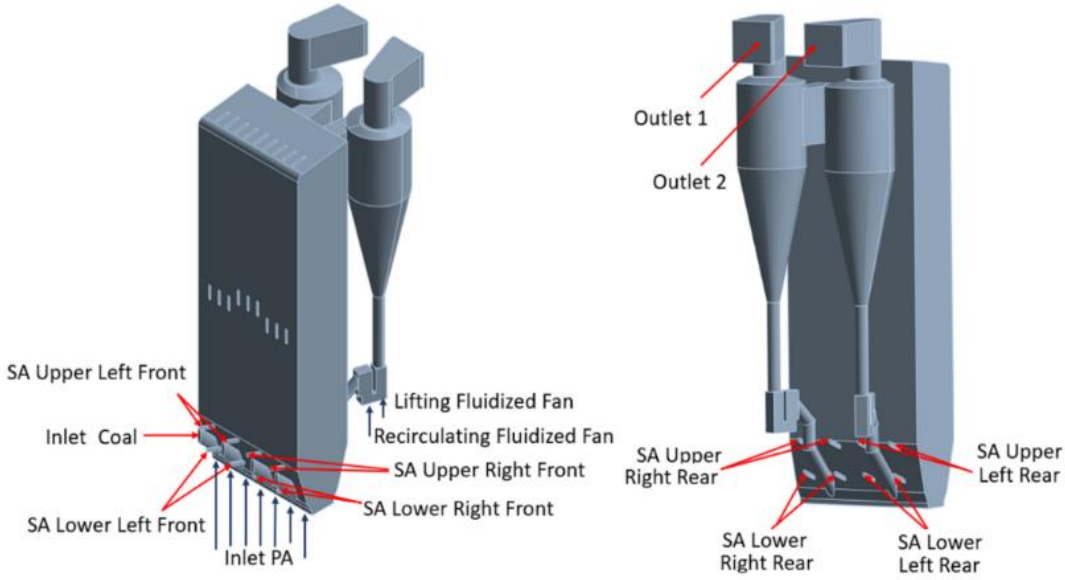

Figure 2. Defining inlet and outlet boundary conditions in the simulation domain

Table 3. Boundary condition of combustion air at the simulation

Boundary Inlet	Initial Pressure (kPa)	Temperature (°C)	Mass flow (kg/s)
Inlet Primary Air	8,6	230	31,69
Inlet coal air (spreading + seal)	9,1	45	8,8
Secondary Air Lower Right-Front	4,0	233	3,53
Secondary Air Lower Right-Rear	3,9	233	3,77
Secondary Air Lower Left-Front	3,6	206	3,62

Boundary Inlet	Initial Pressure (kPa)	Temperature (°C)	Mass flow (kg/s)
Secondary Air Lower Left-Rear	3,5	223	3,22
Secondary Air Upper Right-Front	3,9	233	3,37
Secondary Air Upper Right-Rear	3,9	229	4,57
Secondary Air Upper Left-Front	3,5	214	3,06
Secondary Air Upper Left-Rear	3,4	222	3,91
Lifting Fluidized Fan	0,15	30	0,204
Recirculating Fluidized Fan	0,95	30	0,475

3. RESULTS AND DISCUSSIONS

3.1. Model Validation

To validate the numerical model, a global mass conservation check was performed using the Flux Reports in ANSYS™ Fluent. The DPM Mass Source yielded 0,12 kg/s, reflecting the phase change of coal particles into gas via moisture evaporation and devolatilization. The net mass imbalance (Net Results) was calculated at -0,046 kg/s, attributed to minor residual fluctuations and gas-particle coupling synchronization. Relative to the total inlet mass flow rate of 71,77 kg/s, this discrepancy corresponds to an error of only 0,064%. Being well below the 1% standard tolerance threshold, the law of mass conservation is fully satisfied.

The second validation method was carried out to assess the reliability of the model in projecting actual operating conditions by directly comparing the simulation outputs with real temperature data from the plant's Distributed Control System (DCS). The numerical temperature sampling points were precisely aligned with the physical locations of the field sensors in the furnace, specifically at heights of 0.8 m, 16.6 m, and 31.6 m, as well as the cyclone outlet area. A comprehensive summary of this comparison—comprising the sensor measurements, mean simulated temperatures, and their corresponding percentage deviations or errors—is detailed in Table 4.

Table 4. Comparison of temperature measurements with airfiring simulation results

Location	Measured Temperature (°C)	Simulation Temperature (°C)	Error (%)
Elevation 0.8	873,64	884,63	1,3
Elevation 16.6	822,65	797,21	3,1
Elevation 31.6	654,95	644,54	1,6
Outlet	685,00	651,55	4,9

3.2. Numerical result

The numerical simulation results elucidate the thermodynamic and fluidization shifts during the transition from conventional air-firing (21% O_2 + 79% N_2) to oxy-fuel combustion configurations (21% O2 +79% CO_2). These variations offer critical insights into combustion chamber behavior, fluidization regimes, and potential operational hazards when scaling up to a physical CFB unit.

3.2.1. Thermal profiles

Two-dimensional (2D) contour analysis within the combustion chamber bed area plays a pivotal role in evaluating the thermal and hydrodynamic characteristics of a CFB system. Although quantitative mean values effectively provide macro-level insights into reactor

performance, a solitary average value frequently masks localized anomalies occurring within the dense phase zone. Through 2D contour visualization, the intricate spatial variations in heat distribution inside the boiler can be mapped to uncover the underlying physical phenomena. The visualization of the furnace bed lateral temperature contours is presented in Figure 3.

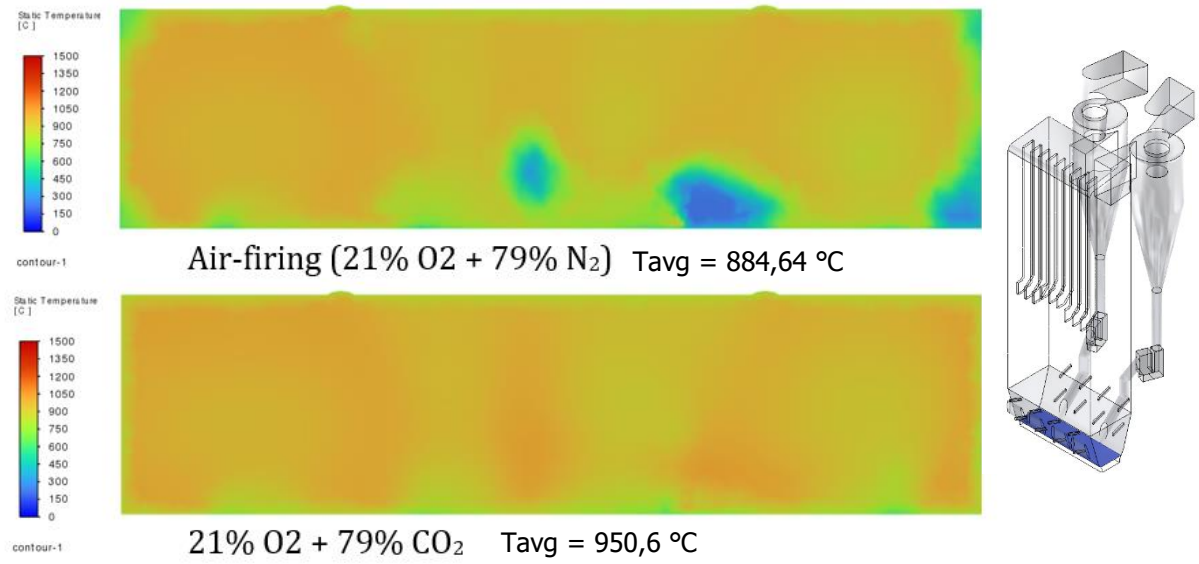

Figure 3. Furnace bed lateral temperature contours

Integrating the 2D temperature distribution contours with the quantitative mean values clearly illustrates the dramatic shift in thermal and hydrodynamic behavior inside the CFB dense bed during the transition to oxy-fuel combustion. Under air-firing conditions, the mean bed temperature is maintained at 884.64°C, representing the optimum thermal window for effective the mitigation of thermal NO_x generation. Conversely, in the Oxy21/79 case, substituting N_2 with CO_2 from the RFG induces an immediate estimation up to 66°C thermal spike, raising the bed temperature by 7.45% to 950.6°C despite maintaining an identical 21% O_2 concentration. Figure 4 illustrates the vertical maximum temperature distribution along the furnace height, spanning from the distributor grid (0 m) to the furnace exit (35 m), comparing conventional air-firing with oxy-fuel combustion case. At the grid plate level, all thermal profiles originate at approximately 230℃ reflecting the inlet temperature of the primary gas stream.

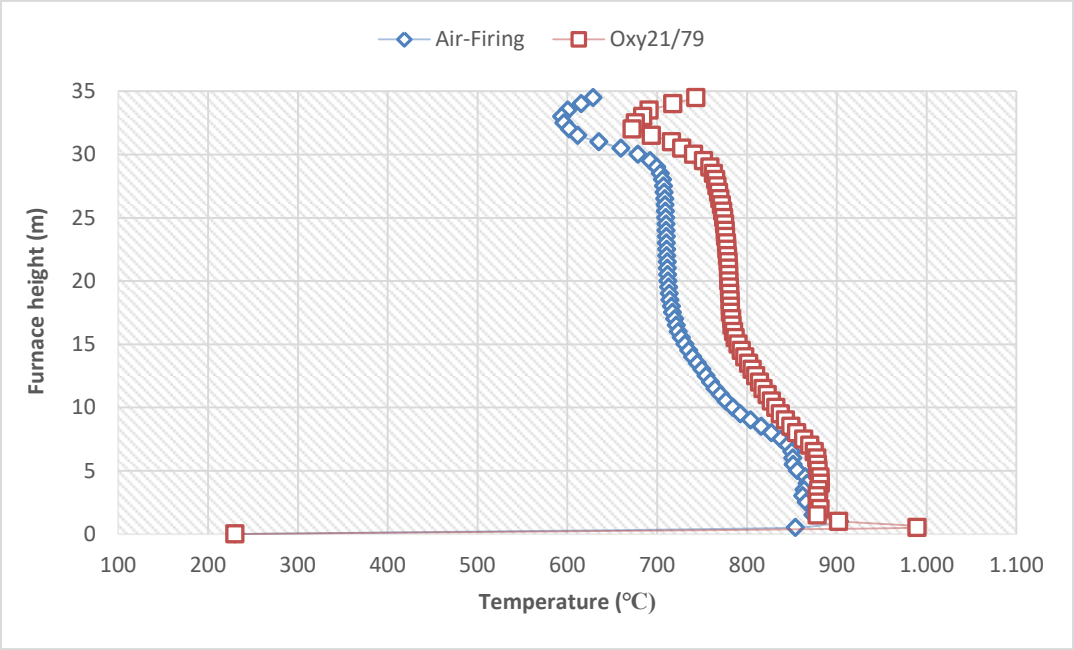

Figure 4. Maximum temperature profile against furnace height

Directly above the distributor, an intense thermal surge occurs as volatiles and char ignite, leading to pronounced temperature stratification in the dense bed region that correlates with oxygen concentration. Throughout the furnace elevation, the Oxy21 mode exhibits a consistently elevated temperature profile compared to the Airfuel baseline. In the lower bed zone ($y < 5$ m), both cases undergo rapid heating; however, Oxy21 develops a substantially higher thermal peak exceeding 990℃, whereas Airfuel peaks near 850℃. As combustion gases rise through the mid-furnace section (5-25 m), temperatures under Oxy21 gradually decline from roughly 880℃ to 775℃, yet remain distinctly above the Airfuel profile, which stabilizes between 850 to 710℃. Toward the upper furnace exit (25-35 m), the Oxy21 temperature slightly rebounds to around 740-670℃, while the Airfuel mode maintains a lower, steady outlet temperature near 630-600℃. This overall thermal enhancement under Oxy21 conditions stems primarily from replacing N_2 with recirculated CO_2 alongside superior gas radiative properties.

The temperature surge encountered when transitioning from air-firing to Oxy21/79—irrespective of the constant 21% oxygen volume—presents a complex hydrodynamic and thermodynamic phenomenon in CFD modeling. This temperature anomaly is primarily driven by three interacting factors.

- Attenuated Solids Circulation Rate
  In CFB architectures, the thermal equilibrium of the lower furnace is heavily regulated by the upward transport and recirculation of bed material (sand and ash). Under air-firing, a superficial velocity of 4.43 m/s coupled with a mass flow rate of 31.69 kg/s at primary air provides sufficient aerodynamic drag to sustain a high solids holdup and continuous entrainment, effectively conveying thermal energy from the lower bed to the freeboard. In contrast, the Oxy21/79 condition exhibits a reduced superficial velocity of 4.33 m/s due to reduction of primary air mass flow rate to 31.13 kg/s. This momentum deficit diminishes the gas phase's lifting capacity, thereby reducing the rate of cooler solids returning from the cyclone. Consequently, the thermal energy liberated from coal combustion becomes confined within the dense phase, driving the localized bed temperature upward.
- Diminished Sensible Cooling by Primary Air (PA)

The primary air stream entering the plenum acts as a vital heat sink for the high-temperature bed material. The capacity of this gas to absorb sensible heat is a function of its mass flow rate and specific heat capacity, governed by $\dot{m} \cdot C_p$. At an inlet temperature of 230°C, the C_p of CO_2 is lower than that of N_2. The oxy-fuel blend suffers a 15% reduction in total sensible heat absorption capacity upon initial bed contact. This decay in the convective cooling effect directly precipitates the bed temperature surge.

- Altered Volatile Combustion Kinetics and Gasification Pathways
  Despite an identical O_2 mole fraction of 21%, the bulk density of the Oxy21/79 mixture is substantially higher due to the molecular weight differential between CO_2 (44 g/mol) and N_2 (28 g/mol). This elevated density, operating under a lowered linear velocity of 4.33 m/s, alters the local mass transfer coefficient and restricts oxygen diffusion toward the coal particle surfaces. Furthermore, the high concentration of CO_2 surrounding the dense phase promotes endothermic char gasification, generating in-situ Carbon monoxcide (CO). This localized CO rapidly consumes the adjacent oxygen, shifting the zone of homogeneous volatile combustion entirely into the lower bed rather than allowing it to distribute evenly along the freeboard height. This concentrated chemical heat release underpins the localized thermal runaway in the bed zone.

The rise in average bed temperature from 884.64℃ to 950.6℃ carries critical operational implications for the CFB boiler. On one hand, the elevated thermal profile within the upper furnace zone delivers higher heat energy, potentially boosting superheated steam generation or requiring precise tuning of the attemperator spray flow to prevent steam temperature overshoots. Conversely, maintaining an average bed temperature around 950.6℃ narrows the margin toward the ash fusion temperature threshold typical of low-rank coals (1050-1100℃). Consequently, rigorous monitoring of localized hotspots is imperative to prevent bed material agglomeration and severe defluidization issues.

3.2.2. Analysis of combustion products : Carbon dioxide

Analyzing the mole fraction distribution of combustion products, particularly CO_2, is crucial for evaluating both the combustion efficiency and the environmental readiness of a boiler system. Spatially mapping these mole fractions within the reactor provides a realistic representation of the underlying reaction dynamics and the exact zones where chemical reactions take place. The simulation CO_2 mole fraction visualizations demonstrating the transition from conventional air-firing to oxy-fuel combustion are presented in Figure 5.

The vertical axial mole fraction contours reveal a pronounced contrast between conventional air-firing and the three oxy-fuel combustion cases. Note that dual contour scales are utilized in the visualization: the left scale (0.00-0.10) corresponds to the air-firing baseline, whereas the right scale (0.00-0.60) represents the oxy-fuel configurations. Under conventional air combustion, the CO_2 concentration remains remarkably low, yielding an outlet mole fraction of merely 0.043 (or 4.3%). This dilution stems primarily from the high volume of atmospheric nitrogen (N_2) introduced through the combustion air. As N_2 serves as the dominant inert carrier gas, the CO_2 distribution across the freeboard appears uniform, as reflected by the light green contour (0.04 – 0.05).

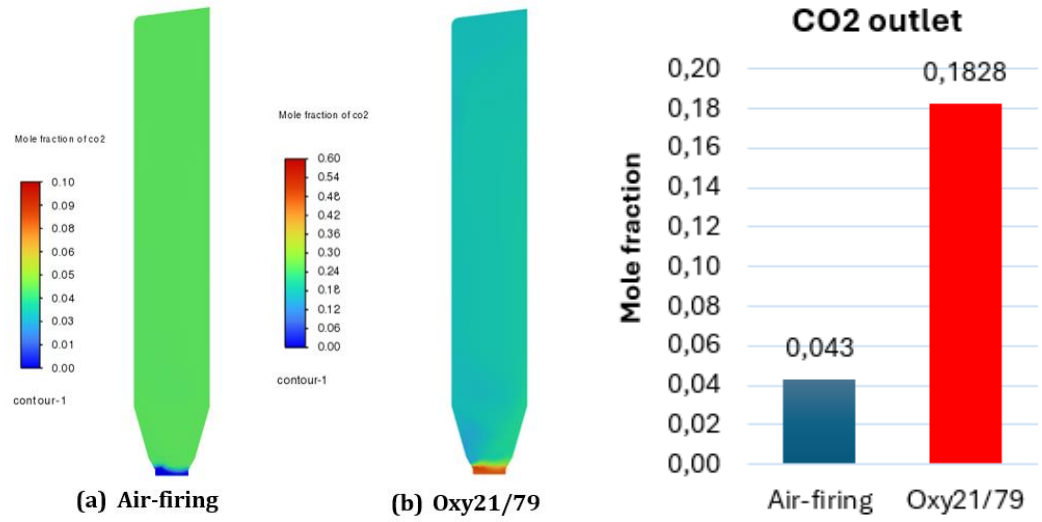

Figure 5. Mole fraction of CO_2 in Furnace and at cyclone outlet

Transitioning to the oxy-fuel regime induces a substantial surge in the overall CO_2 mole fraction throughout the combustor. These results are in good agreement with earlier studies by Yang et al. (2020), Li et al. (2024), and Dong et al. (2024). Replacing ambient air with a mixture of pure oxygen and CO_2-rich RFG effectively eliminates N_2 from the system, directly enriching the flue gas CO_2 concentration. At the bottom inlet, represented by the orange-to-red contours on the right scale, the CO_2 mole fraction peaks between 0.48 and 0.54, marking the entry zone of the recycled gas stream prior to mixing with additional combustion products higher in the furnace. Quantitatively, the simulation results demonstrate a massive jump in exit CO_2 levels upon switching to oxy-fuel combustion. While baseline air-firing produces minimal CO_2 fractions due to nitrogen dilution, shifting to the Oxy21 configuration leads to a dramatic 325.12% increase (more than a threefold surge) in outlet CO_2 concentration. Driven by N_2 exclusion and flue gas recirculation, these contour maps visually confirm that oxy-fuel combustion successfully concentrates CO_2 within the furnace, greatly enhancing suitability for downstream carbon capture. A higher CO_2 density reduces the volumetric flow rate of non-condensable gases, allowing for a more compact and cost-effective Carbon Capture and Storage (CCS) compression unit.

3.2.3. Analysis of combustion products : Sulfur dioxide

Analysis of the movement of the SO_2 mole fraction throughout the furnace is an important instrument because it is useful for depicting the phenomenon of sulfidation as a local accumulation of excessively concentrated sulfur gas near the combustion chamber wall which is the main cause of accelerated material depletion rates and the risk of waterwall pipe leakage. The simulated SO_2 mole fraction visualizations demonstrating the transition from conventional air-firing to oxy-fuel combustion are presented in Figure 6.

In the Oxy21/79 case, the contour profile is predominantly characterized by light-to-dark blue hues throughout the freeboard zone. This provides visual evidence that the Oxy21/79 condition yields the lower SO_2 emissions compared to investigated case conventional air-firing. Although a minor red accumulation is observable at the lower right section of the bed—marking the initial sulfur release zone from the coal matrix—this emitted SO_2 gas is successfully captured within the lower dense region, remaining minimal as it flows upward. Conversely, under the conventional air-firing condition, the concentration contours are dominated by a homogeneous green color across the freeboard, indicating a moderate level

of SO_2 emissions. This behavior aligns with the findings of Kiga et al.(1997) and Croiset et al.(2000), who observed that the conversion rate of coal sulfur into SO_2 decreases during O_2/CO_2 combustion compared to traditional air-firing. The reduction of SO_2 emissions during oxy-fuel combustion is primarily driven by SO_3 formation and subsequent sulfur retention, where a substantial portion of sulfur is absorbed by the in-system ash.

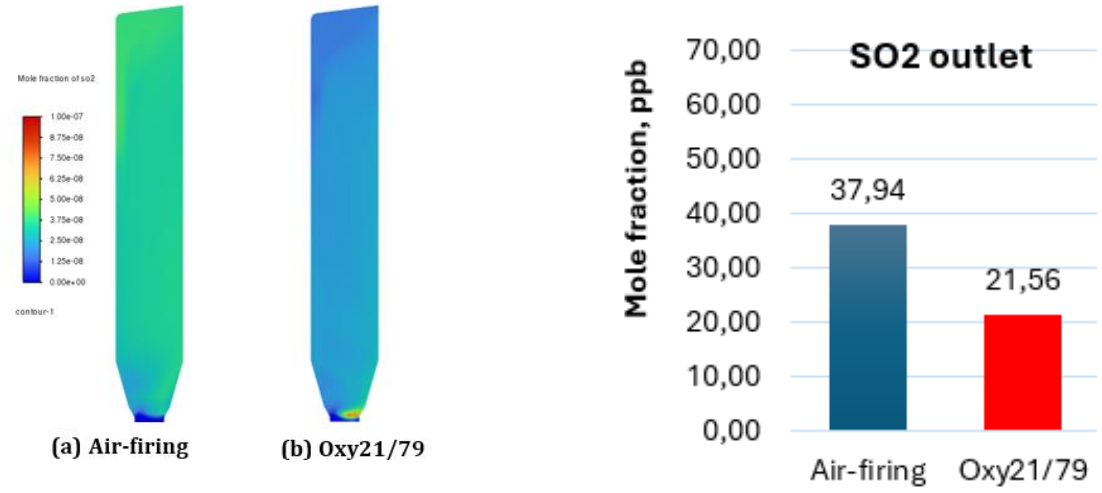

Figure 6. Mole fraction of SO_2 in Furnace and at cyclone outlet

Based on the simulated outlet SO_2 mole fraction data presented in also Figure 6, the emission trends transitioning from Air-firing to Oxy21/79 significantly reduces outlet SO_2 emissions. The SO_2 mole fraction decreases from 37.94 ppb under air-firing conditions to 21.56 ppb under Oxy21/79, representing a 43.17% reduction. This sulfur suppression is primarily driven by enhanced self-desulfurization reactions and increased sulfur retention within the system due to flue gas recirculation (RFG). Re-introducing flue gas extends the residence time of sulfur species, boosting self-desulfurization via alkaline ash components (CaO/MgO). Lower baseline SO_2 emissions mean limestone feeding rates can be optimized, reducing operational expenditure associated with sorbent consumption and bed material turnover.

3.2.4. Analysis of combustion products : Nitrogen oxide

Analysis of the mole fraction distribution of nitrogen oxides (NO_x) along the height of the boiler furnace has a very important meaning in mapping the formation mechanism as well as the reduction pathway of pollutants during the combustion process. The spatial profile of the mole fraction concentration of NOx pollutants helps detect areas where massive conversion of Fuel NO_x occurs (both from volatile nitrogen and char) and detects the potential emergence of Thermal NO_x due to local hot spots and to determine the elevation position where the peak concentration of NO_x occurs provides a technical basis in adjusting the ratio and position of secondary gas injection to create fuel-rich conditions to optimally suppress pollutant formation. The simulation NO_x mole fraction visualizations demonstrating the transition from conventional air-firing to oxy-fuel combustion are presented in Figure 7.

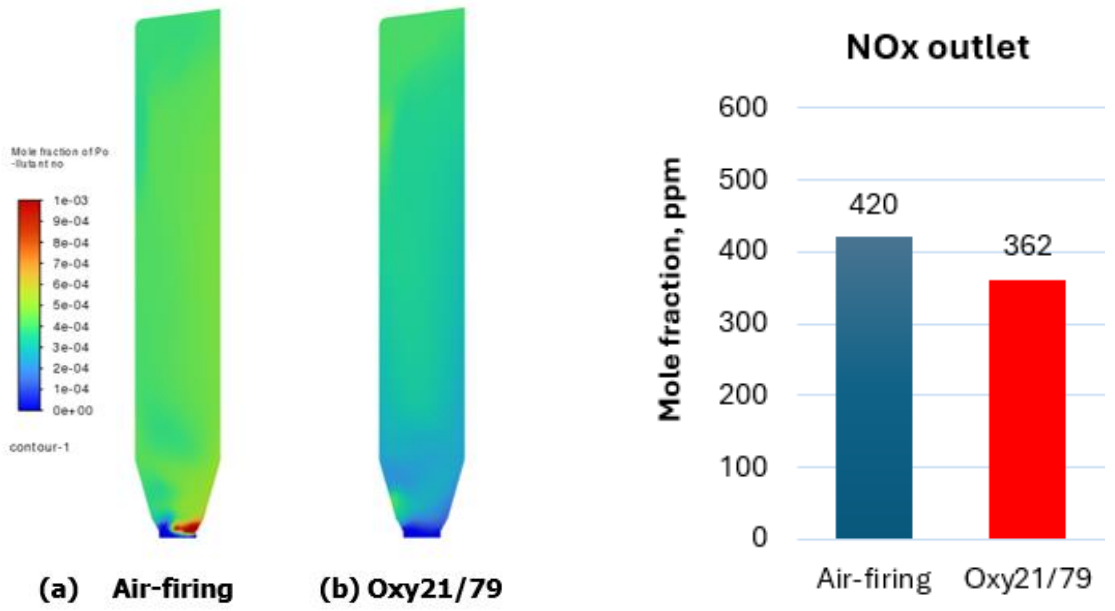

Figure 7. Mole fraction of Pollutant NO_x in Furnace and at cyclone outlet

In the Air-firing case, the contour is dominated by light green along the freeboard with a few red dots at the rear base where the coal first burns. As shown also in the Figure 7, the outlet emission value is at 420 ppm. In this condition, NO_x is mainly formed from the combustion of the inherent nitrogen content of coal (Fuel NO_x) under the supply of nitrogen-rich free air N_2). Furthermore, in the case of Oxy21/79, there is a decrease in pollutant when switching to oxy-fuel, the freeboard color contour begins to cool to light blue/cyan, and the emission value drops to 362 ppm. The disappearance of N_2 gas from the primary air combustion air instantly cuts off the formation path of thermal NO_x and prompt NO_x.

In the oxy-combustion system, flue gas is recirculated into the boiler. This means that the NO gas formed in the previous cycle is forced back into the lower dense bed zone, which is rich in carbonaceous solids (char). Under the moderate temperature conditions of Oxy21 (950.6°C) a highly favorable heterogeneous reduction reaction occurs, named NOx reburning as follow :

$$NO + Char\ (C) \rightarrow N_2 + CO/CO_2 \quad (14)$$

The NO gas is re-decomposed into ordinary nitrogen gas (N_2) by reducing radicals in the bed area. This reburning effect is effective in the Oxy21/79.

4. CONCLUSIONS

The simulation results indicate that adopting the Oxy21/79 configuration is the viable strategy for industrial application. These operating modes yield elevated CO_2 concentrations at the outlet, so providing a highly favorable baseline for subsequent carbon capture operations. Moreover, these operating windows successfully minimize environmental liabilities by suppressing both SO_2 and NO_x emissions. Although both the bed and boiler outlet temperatures increase, switching the combustion mode to oxy-fuel with RFG remains within safe operational limits, with the average bed temperature not exceeding 1050°C. However, localized hotspots reaching 990°C do occur, raising concerns regarding the potential for bed clinkering and localized SO_2 spikes resulting from desulfurization failure.

Based on the present findings, several recommendations are outlined for future research. First, dynamic (transient) simulations should be developed to map the transition from conventional air-fuel combustion to oxy-fuel mode, which is crucial for identifying critical operational thresholds and formulating safety mitigation strategies. Second, experimental or numerical investigations should explore flue gas recirculation control, oxygen staging, and heat exchanger surface modifications to mitigate clinkering risks. Third, further study is required to determine the optimal O_2/CO_2 mixture ratio to effectively suppress localized bed temperature surges at critical locations.

ACKNOWLEDGEMENT

The authors would like to thank the Operations Division at the Pulang Pisau Power Plant for sharing the boiler design drawings, operational data, as well as the coal and sand material analysis. Special thanks are also due to the Department of Mechanical Engineering at Institut Teknologi Sepuluh Nopember (ITS) for the computational resources provided for this study. Furthermore, appreciation is extended to PT PLN (Persero) for funding this research.

5. REFERENCES

Ansys. (2025). Ansys Fluent Theory Guide (Release 2025 R1). Ansys, Inc.

Bryden, K. M., Ragland, K. W., & Kong, S.-C. (2022). Combustion engineering (3rd ed.). CRC Press. DOI : 10.1201/b22232

Buhre, B. J. P., Elliott, L. K., Sheng, C. D., Gupta, R. P., & Wall, T. F. (2005). Oxy-fuel combustion of coal: A review. Progress in Energy and Combustion Science, 31(4), 283–307. https://doi.org/10.1016/j.pecs.2005.07.001

Chang, J., Ma, X., Wang, X., Li, X. (2023). CPFD modeling of hydrodynamics, combustion and NOx emissions in an industrial CFB boiler. Particuology 81. pp 174-188. https://doi.org/10.1016/j.partic.2022.12.019

Chen, G., Li, S., & Wang, L. (2023). Current investigation status of oxy-fuel circulating fluidized bed combustion. Fuel 342. https://doi.org/10.1016/j.fuel.2023.127699

Cheng, L., Li, K., Yu, Q., & Zhang, Q. (2025). The application of numerical methods in the design of large-size CFB boilers. Applied Thermal Engineering 280, Article 128243. https://doi.org/10.1016/j.applthermaleng.2025.128243

Dong, L., Wang, L., Wen, H., Lin, Z., Yao, Z., Zou, C., Xu, H., Hu, H., Yao, H. (2024) Numerical investigation of the oxy-fuel combustion in the fluidized bed using macroscopic model supported by CFD-DDPM. Journal of Environmental Chemical Engineering 12. https://doi.org/10.1016/j.jece.2024.113959

Indrawan, M, D. (2022). Studi Numerik Karakteristik Aliran dan Pembakaran Furnace PLTU Muara Karang dengan Variasi Kadar O2 pada Udara Pembakaran. Thesis. Institut Teknologi Sepuluh Nopember.

Kiga, T., Takano, S., Kimura, N., Omata, K., Okawa, M., Mori, T., & Kato, M. (1997). Characteristics of pulverized-coal combustion in the system of oxygen/recycled flue gas combustion. Energy Conversion and Management, 38(Suppl.), S129–S134. https://doi.org/10.1016/S0196-8904(96)00258-0

Krzywanski, J., Sztekler, K., Szubel, M., Siwek, T., Nowak, W., Mika, L. (2020). A Comprehensive, Three-Dimensional Analysis of a Large-Scale, Multi-Fuel, CFB Boiler Burning Coal and Syngas. Part 1. Numerical Simulations of Coal and Syngas Co-Combustion. https://doi.org/10.3390/e22090964

Krzywanski, J., Sztekler, K., Szubel, M., Siwek, T., Nowak, W., Mika, L. (2020). A Comprehensive, Three-Dimensional Analysis of a Large-Scale, Multi-Fuel, CFB Boiler

Burning Coal and Syngas. Part 2. Numerical Simulations of Coal and Syngas Co-Combustion. https://doi.org/10.3390/e22080856

Leckner, B. dan Gomez-Barrea. A. (2014) Oxy-fuel combustion in circulating fluidized bed boilers. Applied Energy 125, pp 308–318. http://dx.doi.org/10.1016/j.apenergy.2014.03.050 0306-2619

Li, Q., He, F., Mei, S., Xie, J., Zhang, C., Deng, Y. (2024). Effect of oxy-fuel combustion with different O2/CO2 fractions on the pulverized coal combustion mechanism and heat transfer characteristics in rotary kilns: A numerical simulation study. https://doi.org/10.1016/j.cej.2024.153181

Lian, G., Liu, Q., Liu, Y., Zhang, Y., & Zhong, W. (2025). Oxy-fuel combustion in fluidized beds for CO2 capture: Recent advancements in CFD modeling. Carbon Neutral Technologies 1. https://doi.org/10.1016/j.cnt.2025.100004

Ministry of Environment and Forestry. (2021). Indonesia long-term strategy for low carbon and climate resilience 2050 (Indonesia LTS-LCCR 2050). Directorate General of Climate Change, Ministry of Environment and Forestry of the Republic of Indonesia. https://unfccc.int/sites/default/files/resource/Indonesia_LTS-LCCR_2021.pdf

Moran, M. J., Shapiro, H. N., Boettner, D. D., & Bailey, M. B. (2014). Fundamentals of engineering thermodynamics (8th ed.). Wiley.

PT PLN (Persero). (2022). Sustainability report 2021: Optimizing Strategy in Realizing Sustainable Energy Transition https://www.pln.co.id/webapi/media/file/webkorp/asset/SR-PLN-2021.pdf

Tan, Y., Croiset, E., Douglas, M. A., & Thambimuthu, K. V. (2006). Combustion characteristics of coal in a mixture of oxygen and recycled flue gas. Fuel, 85(4), 507–512. https://doi.org/10.1016/j.fuel.2005.08.010

Toftegaard, M. B., Brix, J., Jensen, P. A., Glarborg, P., & Jensen, A. D. (2010). Oxy-fuel combustion of solid fuels. Progress in Energy and Combustion Science, 36(5), 581–625. https://doi.org/10.1016/j.pecs.2010.02.001

Yang, C., Kim, Y., Bang, B., Jeong, S., Moon, J., Mun, T.-Y., Jo, S., Lee, J., & Lee, U. (2020). Oxy-CFB combustion technology for use in power-generation applications. Fuel 267. https://doi.org/10.1016/j.fuel.2020.117206

Zheng, C., & Liu, Z. (2018). Oxy-fuel combustion: Fundamentals, theory and practice. Academic Press, Elsevier. http://dx.doi.org/10.1016/B978-0-12-812145-0.00001-3.